Engineering Failure Analysis 34 (2013) 451–463

Contents lists available at ScienceDirect

Engineering Failure Analysis

journal homepage: www.elsevier.com/locate/engfailanal

Numerical investigation of energy and Reynolds stress distribution for a turbulent flow in an orifice

H.P. Rani [a,*], T. Divya [a], R.R. Sahaya [b], V. Kain [c], D.K. Barua [b]

[a] Department of Mathematics, NIT Warangal, Andhra Pradesh, India
[b] Nuclear Power Corporation of India Limited, NU Bhavan, Anushakti Nagar, Mumbai, India
[c] Material Science Division, Bhabha Atomic Research Center, Mumbai, India

ARTICLE INFO

Article history:
Received 8 June 2013
Received in revised form 22 August 2013
Accepted 27 August 2013
Available online 24 September 2013

Keywords:
Turbulence
Kinetic energy
Dissipation rate
Reynolds stresses
Orifice

ABSTRACT

The turbulent heavy water and light water flows through an orifice, which characterize different reactor systems in nuclear power plants, are studied. The aim was to reveal the influence of process fluid on the turbulence parameters by considering heavy water and light water flows under the unique flow accelerated corrosion (FAC) conditions. The heavy water and light water are referenced based on their density values. The change in density values may have an effect on the flow dynamics and hence on FAC. These effects are brought out in this study and they can be extended to other cases for example, the change in the density of light water due to the chemical additions for controlling the pH values. The flow details at the downstream of orifice were studied extensively with the aid of computational modelling for different Reynolds numbers. Also structural development of the entire vortical flow field which could immensely enhance the knowledge about vortical structures occurring in the recirculation regions at the upstream and downstream of orifice is investigated. This study has been started with the exploration of flow topology of the velocity field by checking the topological consistency. The kinetic energy and dissipation rate were predicted by the modelling of turbulence using the Realizable k–ε model. Also the Reynolds stresses were calculated using the Reynolds stress model. The recirculation region showed maximum value for these parameters near the center line of the elliptic point, but for the dissipation rate this maximum value is observed at the wall. The maximum values of kinetic energy and wall shear stress are observed at the periphery of the orifice in comparison with that of the recirculation region. The predicted turbulent parameters have higher values in the recirculation region for heavy water flow and at the periphery of the orifice for light water flow with respect to each other flows. Also, the *Sh* distribution has been analyzed to estimate the FAC rate along the solid surface. The predicted peak values of these parameters will help to locate the locations which are susceptible to FAC.

1. Introduction

Piping with high velocity water flow experiences flow accelerated corrosion (FAC) rate exceeding 0.1 mm/year at a limited area due to the local area of turbulence [1]. FAC is caused by flow of water and there by dissolution of protective oxide layer of the piping components and then the dissolution of steel by electrochemical action. Generally FAC is characterized by reduction of pipe thickness and is a pipe wall thinning degradation mechanism affecting the carbon steel pipes in power

* Corresponding author.
E-mail address: hprani@nitw.ac.in (H.P. Rani).

1350-6307/$ - see front matter © 2013 Elsevier Ltd. All rights reserved.
http://dx.doi.org/10.1016/j.engfailanal.2013.08.010

plants. FAC may pose a safety and reliability issue in operating plants. FAC has been observed to occur at the downstream of flow-restricting or redirecting components like an orifice, sudden contraction, expansion, elbows, reducers, etc., [2]. Circular orifice pipe flow leads to many instances of thinning degradation/failures in the piping system of thermal power plants/nuclear power plants (NPP) due to FAC. Also, the study of flow separation and its subsequent reattachment to solid surfaces in a circular orifice pipe have attracted many investigations [2,8,12] owing to its importance in various engineering disciplines.

Several catastrophic failures have been reported at several power plants around the world since 1981 due to FAC [3]. At Surry Unit 2 power plant in 1986, severe elbow rupture happened at the downstream of T-bend and caused 4 fatalities. At Millstone 3 in 1990, failure occurred at the downstream of control valves and caused failure of two parallel trains but no injuries. At Louviisa-1 in 1990 failure occurred at the downstream of feeder water systems, without any injuries. At Prairie Power Plant in 1995, FAC failure occurred at the downstream of T-bend and caused two fatalities. At Fort Colhoun in 1997 failure occurred at the bend but no injuries. At Mihama 3 in 2004 failure occurred at the downstream of orifice, caused five fatalities and several injuries. Recently, at Iatan fossil power plant in 2007, failure occurred at the downstream of a control valve, caused two fatalities and a loss of huge capital of plant [2].

The Surry Unit 2 fatal accident [3] resulted in generation of increased interest in FAC, particularly in the high energy piping. The repeated inspections in nuclear power plants have shown that the piping components located at the downstream of flow singularities or flow restricting channels or flow redirecting channels, such as sudden expansion or contractions, orifices, valves, T-bend and elbows are most susceptible to FAC damage. As pointed out [2], this is due to the severe changes in the flow direction as well as the development of secondary flow instabilities at the downstream of these singularities.

FAC is strongly influenced by the fluid velocity, wall shear stress, water chemistry, temperature, piping configuration and alloy content [4,5]. Also, the mass transfer coefficient (MTC) is the most important flow parameter that affects FAC and it depends on the geometry, flow rate, turbulence, surface roughness, void fraction in two-phase flows and physical properties of the transported species in water [1]. The flow and mass transfer analysis in feeder bends under FAC operating conditions was paid attention in literature [1,6,7]. The plant and laboratory (experimental) evidence for the relationship between the local mass transfer conditions and FAC rate were presented [1,6,7]. Also the correlations between the MTC in piping components that are highly susceptible to FAC was paid attention by them. Gammal et al. [8] presented the flow and mass transfer analysis at the downstream of an orifice under FAC conditions. They correlated the FAC rate with the turbulence kinetic energy (TKE) and mass transfer in terms of Sherwood number.

Apart from the feeder bends, the steam generator (SG) components are also subjected to turbulent flow and under such conditions the lifetime may be significantly reduced from their original design life time. Pietralik and Heppner [6] conducted a susceptibility analysis of FAC for tube supports in the recirculating SGs. The ranking of SG locations in the order of FAC susceptibility was estimated from an empirical and Kastner–Riedle model [6]. The effect of local wall thinning on the collapse behavior of pipe elbows subjected to a combined internal pressure and in-plane bending load was investigated by Kim et al. [9]. They evaluated the global deformation behavior of these elbows, which contain various types of local wall-thinning defects at their intrados or extrados. Kain et al. [4,10] and Singh et al. [11] studied the FAC degraded components from NPPs in India and explained the remedial measures for replacement and possible design and water chemistry changes to combat it. They explained the operating parameters such as the pH and the steel containing chromium that help in minimizing FAC to offer longer life under similar operating conditions.

The present study deals with the geometrical aspect of FAC by assuming other important effects i.e., pH, dissolved O_2, etc. are constant. A detailed flow analysis is carried out in an orifice with different fluid flows such as heavy water and light water, since this geometry is reported to have undergone severe FAC degradations leading to failures [2,4,10] in the corresponding reactor systems of NPP. The recirculation region occurring in and around the orifice was analyzed for different Reynolds number (Re) values of heavy water and light water flows, remaining FAC conditions are unique. Usually the FAC/mass transfer can be represented in terms of the Sherwood number and it can be correlated with the simulated TKE [8]. Hence an attempt has been made to analyze the TKE. Also, the variations of other turbulent parameters such as dissipation rate (DR) and Reynolds stresses are clearly identified in the recirculation region at the different axial locations along the transverse direction. The outputs of present simulation facilitate to compare and identify the FAC prone areas across orifice under the considered conditions.

The present paper is organized as follows: In Section 2, a detailed description about the formulation of the problem along with a mathematical model is given. Also, the governing equations, such as, Mass, Momentum, Energy, Species transportation and turbulence equations for the incompressible fluid flow are employed in the considered geometries, along with the boundary conditions. In Section 3, the grid generation and the numerical methods for solving the above governing equations are given. In Section 4, the validation of the numerically simulated results is shown. The flow topology is show for heavy water flow and the Euler number is calculated. The reattachment length, TKE, DR and Reynolds stress distribution are analyzed for both the heavy water and light water flows. Finally, the concluding remarks are made in Section 5.

2. Problem description and mathematical formulation

In the present study two-dimensional, turbulent, steady and fully developed flow in the circular orifice made of carbon steel material with diameter (D) 25.4 mm [12] was considered. The geometry of the physical problems considered in this study along with the coordinate system used is shown in Fig. 1. The tube of length 9D with a circular orifice of inlet height

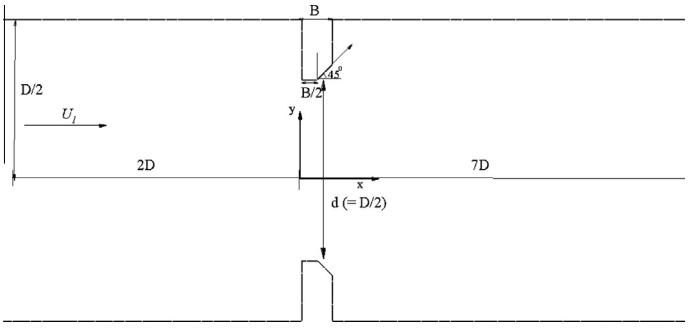

Fig. 1. Cross sectional geometry of an orifice considered in this study, D (25.4 mm), B (3.2 mm) and U_1 denote the inlet diameter, orifice thickness and inlet velocity, respectively.

D is considered. This orifice is assumed to be of thickness (B) 3.2 mm and of diameter $D/2$. The upstream and downstream lengths of flow singularity locations were chosen to be large. Therefore, it is taken that the flow at the inlet is a fully developed flow. These considered lengths reduced the effect of inlet and outlet boundary conditions on the flow patterns in the vicinity of the wall. At the flow singularity locations, these patterns are consistent with other studies in the literature and this validation is shown in Section 4.1.

The turbulent flow of different fluids in the orifice was simulated by using the ANSYS Fluent [17]. The flow is governed by the basic equations such as the conservation of mass, momentum and energy together with the species transport [17].

The flow is considered as steady, thus, the temporal terms have been eliminated. To illustrate the influence of turbulent fluctuations on the mean flow, the flow variable $\boldsymbol{U} = (U_1, U_2)$ is considered to be the sum of mean velocity ($\boldsymbol{u}$) and fluctuating velocity ($\boldsymbol{u}'$) (i.e. $\boldsymbol{U} = \boldsymbol{u} + \boldsymbol{u}'$). Then, the resultant equation for the conservation of mass is given by

$$\nabla \cdot \boldsymbol{u} = 0 \tag{1}$$

The Reynolds time averaging equation for momentum is given by

$$(\boldsymbol{u} \cdot \nabla)\boldsymbol{u} = -\frac{\nabla p}{\rho} + v\nabla^2\boldsymbol{u} - \nabla \cdot \overline{(\boldsymbol{u}_i'\boldsymbol{u}_j')} \tag{2}$$

where ρ is the density, p is the static pressure, v is the kinematic viscosity of the fluid and $\overline{(\boldsymbol{u}_i'\boldsymbol{u}_j')}$ is the turbulent shear stress or Reynolds stress. The convention of this notation is that i or $j = 1$ corresponds to the x-direction, i or $j = 2$ the y-direction. By using the Boussinesq theorem, $\overline{u_i'u_j'}$ in Eq. (2) is proportional to the average velocity gradient, can be calculated as

$$\overline{u_i'u_j'} = v_t\left(\frac{\partial \boldsymbol{u}_i}{\partial x_j} + \frac{\partial \boldsymbol{u}_j}{\partial x_i}\right) = v_t E_{ij} \tag{3}$$

where v_t is the turbulent viscosity. This viscosity was calculated using different turbulence models and these models are discussed in the next subsection. Eqs. (1) and (2) were solved along with the following energy equation

$$\nabla \cdot (\boldsymbol{U}T) = \frac{1}{\rho}\nabla \cdot (k_{eff}\nabla T) \tag{4}$$

where T denotes the temperature, k_{eff} is given by $k_t h + C_p\frac{\mu_t}{Pr_t}$, with turbulent Prandtl number $Pr_t = 0.85$, k_{th} denotes the thermal conductivity, C_p is the specific heat at constant pressure and μ_t is the eddy viscosity.

The conservation equation of the chemical species, which predicts the local mass fraction of species (ferrous ions), takes the following general form:

$$\nabla \cdot (\boldsymbol{U}Y) = \frac{\nabla \cdot J}{\rho} \tag{5}$$

where the mass diffusion flux of species is defined as $J = \left(\rho D_1 + \frac{\mu_t}{Sc_t}\right)\nabla Y$, with constant turbulent Schmidt number ($Sc_t = 0.7$), Y is the local mass fraction of the species and D_1 is the diffusion coefficient of the species.

Also to model the turbulent flow, the Realizable k–ε [13,17] and Reynolds stress turbulence models [15,17] are employed to predict the separated flow and Reynolds stresses, respectively.

2.1. Boundary conditions

In the present study, the employed boundary and FAC conditions are similar to that of used by Pietralik and Schefski [7]. Two different fluid flows are considered namely, heavy water and light water. The uniform velocity and Neumann boundary condition for the pressure variable are used as the inlet boundary conditions. The constant temperature as the thermal boundary condition, constant concentration of the species and no-slip conditions are imposed on the wall. At the outlet,

the zero-gradient properties are considered to be linear for pressure. The axial symmetry is considered for all the geometries. For the FAC conditions the critical temperature was considered to be 310 °C and the $Sc(=\frac{\nu}{D})$ was chosen as 9.2 for the modelling as used by Pietralik and Schefski [7]. The simulations were carried out for the three $Re(=\frac{U_1 D}{\nu})$ values based on the uniform inlet velocity (U_1) values namely, 2e+4, 4e+4 and 6e+4 to analyze the flow. For heavy water and light water flows ν was chosen to be 1.131e−6 (m^2/s) and 1.004e−6 (m^2/s), respectively. The transitional non-dimensional wall roughness height, $k_s^+(=\frac{\rho k_s u^*}{\mu})$ is considered to be 2.8, with roughness height k_s(=7.5e−5). In the above definition u^* represented as $\frac{U_1}{u^+}$ and in the log law layer (as $y^+ < 450$) u^+ is defined as $u^+ = \frac{1}{k} ln y^+ + B$ in which κ is the von-Karman's constant (=0.4) and B = 5.5 [16].

The exit boundary is located sufficiently far downstream from the region of interest; hence an outflow proposed is a fully developed flow as shown in Fig. 2. The Fig. 2 represents the velocity magnitude at Re = 2e+4 along the transverse direction (y) at the axial locations x = 0.177 m and 0.2 m for the downstream lengths of the orifice 7D and 8D, respectively. It is observed from Fig. 2 that increase in the downstream length did not change the flow behavior. Hence the downstream length of 7D is considered to be sufficient for the analysis.

3. Method of solution

The numerical simulation was performed by using the commercial CFD package, namely, ANSYS Fluent 12.1. Fluent uses a control volume technique to solve the governing system of partial differential Eqs. (1)–(5) by constructing a set of discrete algebraic equations with conservative properties. The pressure based numerical scheme, which solves the discretized governing equations sequentially, was selected. Two equation turbulence models to account for high Reynolds number flow considerations, such as realizable k–ε model and Reynolds shear stress model equations were selected. In the sequence of updates, the velocity field was updated through the solution of the momentum equations using the known values for pressure and velocity. The SIMPLE algorithm was used along with the staggered grid to simultaneously solve the velocity and pressure equations. The POWER LAW scheme for the orifice was used as given in the literature [12], for discretising convection and diffusion transports on a uniform grid. Finally, the algebraic equations were solved by using the Guass–Siedel point by point iterative method in conjunction with the algebraic multi grid (AMG) solver. It is well known that the use of AMG method can greatly reduce the number of iterations required to obtain a converged solution, particularly when the model contains a large number of control volumes. A cluster of nodes was generated in the vicinity of the wall i.e., extended up to edge of the wall covering the buffer layer as well as the viscous sub layer. To generate this mesh, the distance between the first calculating node and the wall was chosen to be so small to have $y^+ < 450$ [17] as given in the following relation:

$$\text{First cell height} = \text{R.F.}\left[\frac{y^+ D^{0.125}}{0.199}\left(\frac{\mu}{U_1 \rho}\right)^{0.875}\right] \tag{6}$$

where the R.F. is refinement factor and it was considered to be one for the fine mesh.

In order to obtain an economical and reliable grid system for the computations, a grid independency test has been performed and qualitatively represented in Table 1. It can be observed from this table that the value obtained with the currently employed grid system of 130,610 nodes, differ by 1% with the grid system of 64,672 nodes (approximately half of 130,610 nodes) and differ by 0.4% with the grid system of 253,019 nodes (approximately double of 130,610 nodes). Hence, the grid with the 130,610 nodes had been selected for all subsequent analyses.

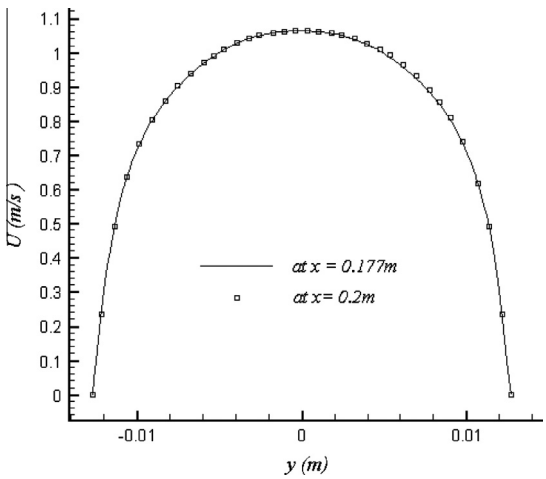

Fig. 2. The velocity magnitude (U m/s) against the vertical coordinate y (m) for different values of x (m) for Re = 2e+4.

Table 1
Grid independence test.

Location of U (m/s)	Total number of nodes	Velocity magnitude U (m/s)	Difference/%
(0,0.1)	64,672	1.8817	0.0098/1
	130,610	**1.8719**	
	253,019	1.8675	0.0044/0.4

The convergence criterion was set in between the values from 1e−4 to 1e−6 for the flow variables. About 5e+3 iterations were needed for the satisfactory convergence criteria. The computation was carried out using the workstation HP Z800 Intel Xeon Dual Core Processor.

4. Results and discussion

Water chemistry is the one of the most important parameter influence the FAC [1,7,8]. Hence two different fluid flows, namely, heavy water and light water are considered in the present study and are analyzed under the same FAC conditions and these two fluids represent the two different water that are used in reactors. The density of heavy water and light water differs and this difference have an effect on the flow dynamics and hence on FAC. This study can be further extended to elucidate the change in the density of light water due to the chemical additions for controlling the pH values. The comparison between these two different fluid flows is made with aid of turbulent parameters. The flow topology and the corroborative evidence for the numerical results are shown for the heavy water flow.

We begin by presenting the numerical validation of present numerical results with the results reported in literature. The flow topology is presented to give a global picture of the two dimensional flow developments by checking the topological consistency. Recirculation regions can have significant effects on the TKE close to the wall and this TKE affects the wall shear stress, pressure [2] and wall mass transfer [8]. Hence, the recirculation regions and reattachment points were captured in the flow downstream of the orifice. Also, the turbulent parameters such as TKE, DR and the Reynolds stresses are calculated at different axial locations along the radial direction in the downstream region of orifice.

4.1. Numerical validation

The simulated turbulent air flow in the orifice was compared using the available data in literature and is shown in Fig. 3. This presents the comparison results for the flow in orifice between the results of Smith et al. [12] and the simulations by means of the streamline portrait. It is observed that the comparison between the simulated results and those of Smith et al. [12] are found to be in good agreement. From the portrait, the presence of a recirculation zones can be noticed at the upstream and downstream of the orifice. This secondary flow occurs due to the sudden change in the geometrical configuration which causes several significant changes in the flow parameters and the flow behavior. The present study is about these turbulent flow parameters which are correlated with the mass transfer rate in the recirculation region [18].

4.2. Flow topology

We begin by presenting the flow topology to give a global picture of the two dimensional heavy water flow developments in the orifice at Re = 2e+4. To obtain a profound understanding of the character of the flow structure, we may resort to the topology of streamlines or skin friction lines in order to extract the meaningful flow physics from an enormous amount of computed data. By making use of the kinematic nature of streamlines, the critical points are classified as singular nodes, foci and saddles. This illustration helps us to visualize the global structure of the vortical flow. In Fig. 4, the simulated streamlines along with saddle points, that are located at each critical location such as at the recirculating regions, are presented.

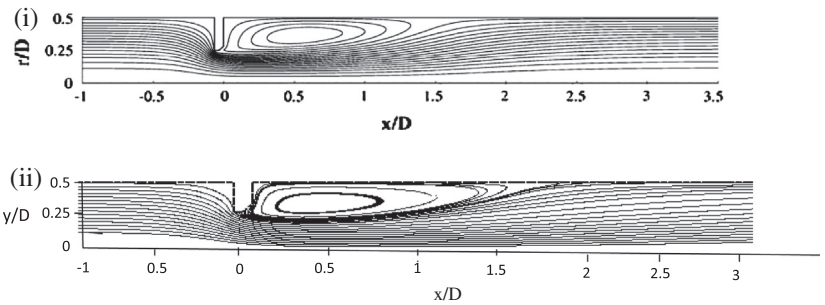

Fig. 3. Comparison between streamlines predicted by (i) Smith et al. [14] and with those of (ii) simulated results.

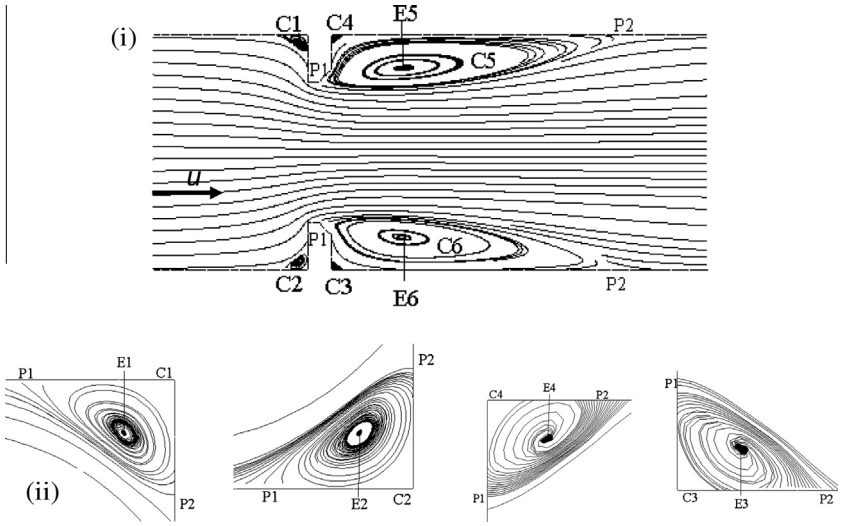

Fig. 4. (i) The simulated steamlines for *Re* = 2e+4 with the corresponding magnified views (ii) at the corners. The critical points *E* and *P* denote the elliptic and parabolic points, respectively, and *C* denotes the recirculation region.

The recirculating regions arise either due to flow separation from stationary walls or due to the formation of separatrix streamlines within the fluid. The points of flow separation or reattachment and the points from which the streamlines in the form of separatrices emanate are the critical points of the flow and require special attention. Elliptic and hyperbolic critical points occur inside the fluid. Fluid elements experience rotational motion about an elliptic point but get stretch and compress about a h yperbolic point. Parabolic critical points occur on the stationary surfaces and for bounded flows; these points always appear in pairs where they are commonly known as the flow separation and reattachment points. Apart from vanishing velocity, the vorticity also vanishes at parabolic points.

These attachment and separation points appeared to be the barriers in the flow field. Along with these points the sign of the direction of the flow has changed: one flow points towards the saddle while the other one points away from the saddle. The region within the points of separation and reattachment hereinafter referred to as the reattachment region and it is of our main interest in the present study. The flow physics and the effects of FAC in these recirculation regions are discussed in detail in the following sections.

4.2.1. Recirculation region

Computational study was carried out to understand the corresponding velocity component in the flow direction adjacent to the bounding walls and downstream from the critical locations for the purpose of locating the reverse flow regions. These lines are used to locate the positions where the axial and transverse shear stress components are zero when the flow is along the *x* and *y*-directions, respectively. The separation flow was characterized by presence of the recirculation region developed at the corners and at the downstream of the critical locations of each component. The recirculation region is analyzed with the help of the simulated streamline portrait. The support for the proposed streamlines portrait was provided by listing the corroborative numerical evidence [12] in Fig. 3 and is discussed in the beginning of this section.

4.2.2. Corroborative evidence for the simulated streamline portrait

Now we understand that the streamline portrait in Fig. 4 is realistic. The simplest topology constraint is based on the Euler number, ξ, of the flow. As explained by Jana et al. [19], the Euler number on the surface is defined as the sum of the Poincare indices of the critical points on the surface. The Poincare index of hyperbolic point is -1, a parabolic point is $-1/2$, and for an elliptic point it is 1. The topological invariance relation is given by

$$\mathrm{NE} - (\mathrm{NH} + (1/2)\mathrm{NP}) = \xi = 0 \tag{7}$$

where the NE, NH and NP represent the number of elliptic points, hyperbolic points and parabolic points, respectively. The topological relation given in above equation itself does not guarantee the existence of the flow therefore it is customary to consider as a way to check the topological consistency. In Fig. 4(i), the counter rotating cells enclosing the elliptic points E_i's are labeled as C_i's. From Fig. 4(i), it is observed that the re-circulating cells clearly delineated at the critical locations. The re-circulating cells at the corners are observed with a magnified view as shown in Fig. 4(ii). Each of these re-circulating cells has an elliptic point at its center. Each elliptic point is bounded by pair of parabolic points (*P*1,*P*2) and no hyperbolic points are seen in these streamline portraits.

Obviously, the streamline portrait, exhibited in the orifice in Fig. 4, satisfies the topological rule given in the above equation with NE = 6, NH = 0 and NP = 12. Though we could validate the simulated velocity field by pursuing the idea that the

physically realizable kinematics of a flow was related to its stability, we focused only on the structural stability mode, however, subjected to the infinitesimal changes to the geometry and boundary conditions in the currently investigated system. Drazin and Reid [20] defined a structurally stable system as the one which did not change in the qualitative character of its solution(s) under the infinitesimal changes of the geometrical and physical parameters of the problem, fluid properties and boundary conditions. The flow depicted in Fig. 4 is structurally stable according to the theorem given by Ma and Wang [21]. Indeed, the conditions for the structural stability criteria of the divergence-free vector fields that satisfy the Dirichlet boundary conditions (no slip at the walls) are met.

The velocity field is sufficiently regular and a parabolic point on the boundary is connected to another parabolic point on the same boundary (in Fig. 4, $P1$ is connected to $P2$ and they are located on the same end wall). The two parabolic points, $P1$ and $P2$ shown in Fig. 4, are connected with the stable manifolds. These manifolds corresponded to the flow regions $C1$–$C6$, which are separated by the counter-rotating cells. These manifolds acted as barriers for the vortices ($E1$–$E6$) when the flow is observed from the inlet. In order to verify whether the flow structure is structurally stable, we had to further corroborate the fidelity of the reconstruction of the velocity field. The support for the proposed streamlines portrait is provided by listing the corroborative numerical evidence of Smith et al. [12] in Fig. 3. There is a good agreement between the present and previously published results [12].

4.2.3. Zero shear stress or flow separation line

Fig. 5 shows the zero shear stress lines of the recirculation regions, $C1$, $C4$ and $C5$, in the upper half of the orifice. Also this figure compares the zero shear stress lines between the heavy water and light water flows. These results are shown for the three different Re values, namely, 2e+4, 4e+4 and 6e+4. As shown earlier in Fig. 4, $C1$ and $C4$ are residing in the upstream and downstream corners of orifice, respectively; the other recirculation region $C5$ is seen at the downstream of the orifice, which is a larger recirculation region in comparison with all other recirculation regions, and it is of our main interest. It can be observed from the zero shear stress lines of $C5$ that each of these lines start with the flow separation at the orifice edge and end at the down-stream of the orifice. The reattachment length of all the recirculation regions increases as Re increases. The reattachment length generated by the light water is higher comparing with that of the heavy water due to the less density and viscosity of the light water.

4.3. Turbulent kinetic energy (TKE) and dissipation rate (DR)

The orifice passage is a typical geometry in which the generation of turbulent energy takes place due to the sudden change of geometrical conditions causing the instability and ultimately culminates in turbulence.

The simulated TKE and DR are plotted in Fig. 6 along the upper solid surface at the downstream of the orifice for heavy water flow and light water flow for different Re. As the flow is axi-symmetric the behavior of all the parameters at the lower surface are assumed to be similar as at the upper surface. It is observed from the Fig. 6 is that TKE and DR increase as Re increases for both heavy water flow and light water flow. The impact of TKE is more in the case of heavy water flow as it is observed in Fig. 6(i) where as the impact of DR is more for the light water flow as it is observed in Fig. 6(ii), when comparing with the other flow. Also observed that the peak of these variables exist at the center of the recirculation region $C5$ and then slowly increasing at the downstream of the recirculation region.

The simulated TKE and DR are plotted in Fig. 7 from the centerline($y/d = 0$) of the orifice to the upper wall ($y/d = 1$) in the recirculation region, $C5$. It is observed that TKE and DR at the center of the orifice have very small values, i.e., in the order of 1e−2. Then they slowly increase as the orifice region is approached and attain the peak. They increase appreciably within the

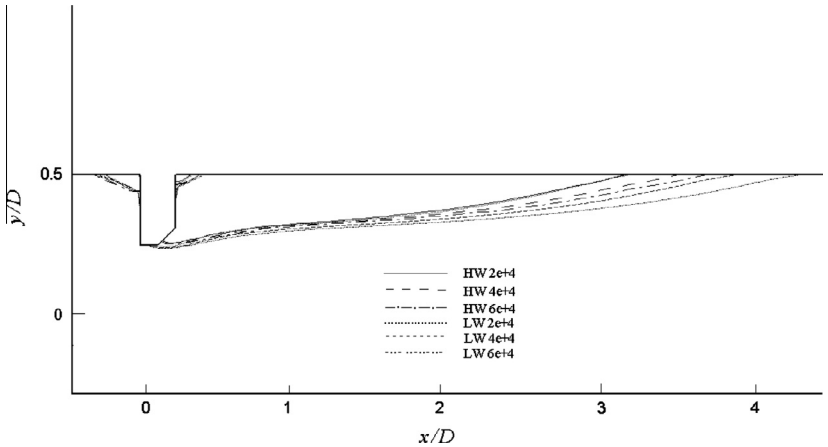

Fig. 5. The simulated zero shear stress lines of heavy water and light water flows.

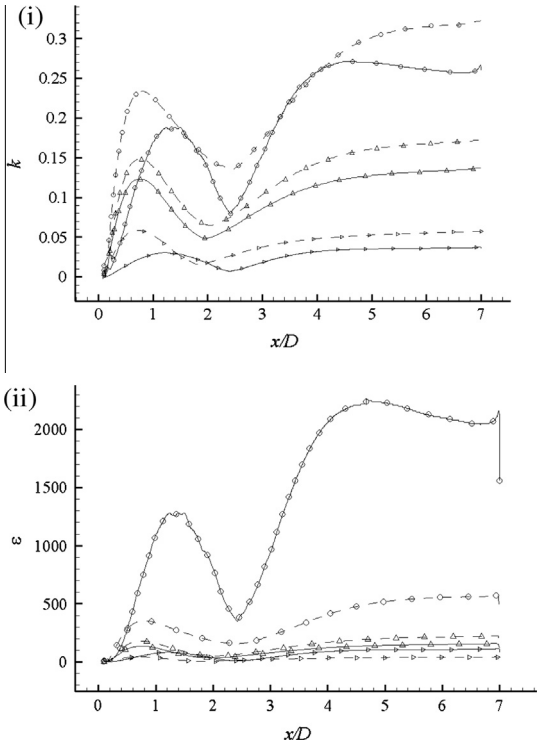

Fig. 6. Simulated profiles of (i) TKE and (ii) DR of heavy water (— —) flow and light water (—) flow for three different *Re* values (▷ 2e+4, △ 4e+4 and ○ 6e+4) along the upper solid wall region at the downstream of orifice.

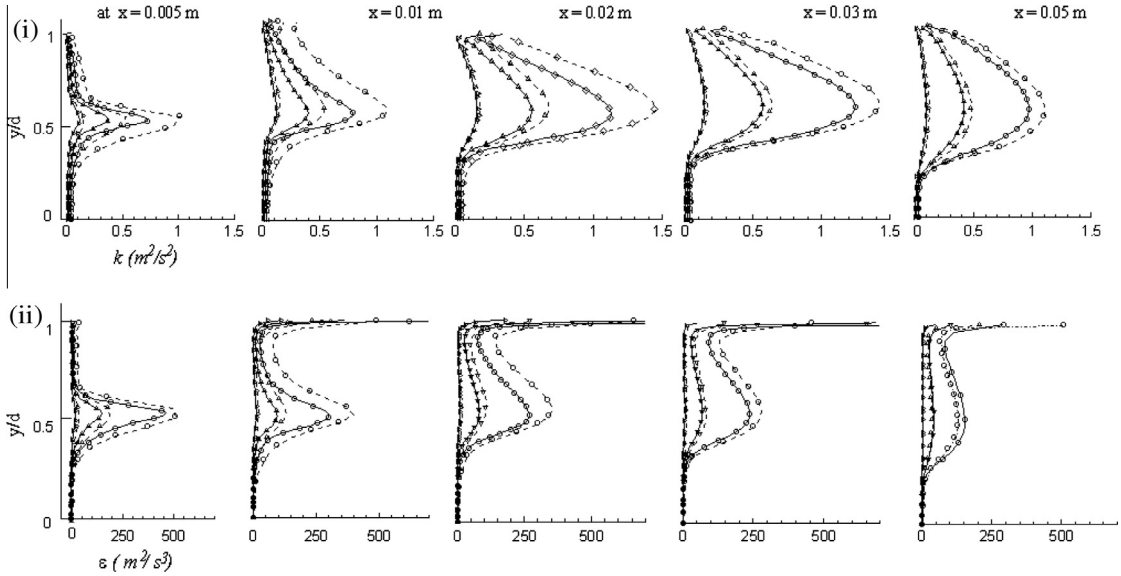

Fig. 7. Simulated radial profiles of (i) TKE and (ii) DR of heavy water (– – –) flow and light water (—) flow for three different *Re* values (▷ 2e+4, △ 4e+4 and ○ 6e+4) at the five axial locations.

flow separation zone due to the presence of high velocity gradients. These peak values are observed at the recirculation region, *C*5, which contains an elliptic point *E*5 (refer Fig. 4). After that they slowly decrease in the vicinity of the wall. This decreasing trend is due to the fact that there exists a laminar sub layer at the wall. In a laminar sub layer the flow is no longer turbulent and the turbulent intensity has to be zero at the vicinity of the wall. Hence this dropping nature of the TKE is phys-

ically possible. But the DR shows the higher values at the wall than the previously observed peak values. For both heavy water and light water flows the generation of the TKE approximately starts from the region of the passage where the geometry of the passage changes.

Fig. 7(i) shows the radial profiles of the TKE for three different *Re* values at five different streamwise locations in *C*5. These profiles are observed to be qualitatively similar for all the *Re* values. The local peak values of TKE increases as *Re* increases. The location of these peak values has been strongly influenced by the elliptic point E5. Thus, the maximum TKE occurs in the centerline of the recirculation region. After that the TKE is in the decreasing trend while moving towards the solid wall where there is a laminar sub layer. As the axial location is chosen away from the orifice (i.e., from x = 0.005 m to 0.05 m), it is observed that the peak value of the TKE increased until the axial location is close to the elliptic point (*E*5) and then it get decreased. The same observation was made by Ahmed et al. [18] for the circular orifice. Ahmed et al. [18] correlated MTC distribution with the TKE in the recirculation region at the downstream of the orifice. Therefore the MTC distribution resembles the TKE distribution. Also observed form the present results is that heavy water flow have the high TKE when comparing with that of the light water flow in the corresponding locations.

Fig. 7(ii) shows the profiles of the DR for the three different *Re* values at five different axial locations. These profiles, within the recirculation region, are observed to be qualitatively similar for all the considered *Re* values. These local peak values of DR, as well as its radial location from the wall, increase as *Re* increases. For x = 0.005 m, the maximum DR is observed at the center of the recirculation region instead of at the wall because of the presence of the recirculation region *C*4. While for the remaining axial locations i.e., for x = 0.01–0.05 m, this DR is maximum at the upper wall, where the kinetic energy is zero/minimum [22]. Specifically for the *Re* = 6e+4 the DR is drastically increased at the upper wall. At the wall the light water flow has higher DR comparing with that of the heavy water flow and at other regions this trend is reversed.

4.4. Reynolds stresses

In general for a low Reynolds number flow the viscous stresses dominate at the wall compared with Reynolds stresses, in contrast to the other locations. The no-slip condition dictates that all the Reynolds stresses are zero at the wall. But for higher Reynolds numbers the viscous stresses are everywhere negligible and small compared with the Reynolds stresses. Hence in the present study these Reynolds stresses have been analyzed for the considered high turbulent flow [22].

The simulated Reynolds stresses are plotted in Fig. 8 along the upper solid surface at the downstream of the orifice for heavy water flow and light water flow for different *Re*. It is observed from the Fig. 8 that shear and normal stresses increased

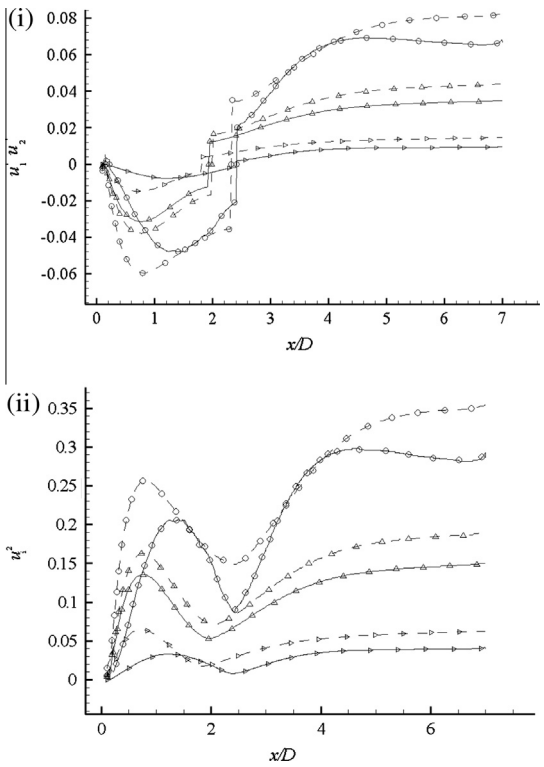

Fig. 8. Simulated profiles of (i) Reynolds shear stress and (ii) normal stresses of heavy water (— —) flow and light water (—) flow for three different *Re* values (▷ 2e+4, △ 4e+4 and ○ 6e+4) along the upper solid wall region at the downstream of orifice.

as *Re* increases for both heavy water flow and light water flow. Both of these stresses have more values for the heavy water flow comparing with the light water flow. The shear stress is negative in the recirculation region; at the reattachment point the sign of the stress is changed to positive value and then after having positive values for both the flows and it can be observed in the Fig. 8(i). The negative peak value of shear stress exists at the center of the recirculation region and at the downstream of the recirculation region slowly increasing with the positive values. The normal stress is having the positive values trough out the solid surface, having the peak values at the center of the recirculation region and at the downstream region increasing.

The radial profiles of the Reynolds stresses such as shear stress and normal stress are shown in Fig. 9 at five streamwise locations in the recirculation region ($C5$) for different *Re* values. On the centerline of the orifice, both of these Reynolds stresses are zero. Fig. 9(i) and (ii) show the Reynolds shear stresses and Reynolds normal stresses, respectively. The amplified *Re* results in the increase of both shear and normal stresses at all the axial locations. From Fig. 9(i), it can be observed that along the transverse direction in each axial location, the Reynolds shear stress increases, attains a maximum value at the center of the mixing layer, decreases in vicinity of the wall and finally at the wall there is a small amount of negative shear stress. Similar observation can be seen from Fig. 9(ii) for the Reynolds normal stress. But, at the vicinity of the wall it reaches the minimum value and at the wall small amount of increment in it has been observed. Heavy water flow showed more Reynolds stress value comparing with that of the light water flow.

4.5. Wall shear stress (τ)

The fluid flowing on the wall surface of a pipe at a high velocity erodes the corroded surface mechanically due to the shear force on the surface by the fluid. Most of the factors, except the hydrodynamic factors such as the flow velocity and the shear stress, uniformly affect the whole inner surface of the piping system through which the fluid flows [5]. The effect of wall shear stress has been analyzed at the wall of cross sectional orifice. The wall shear stress and the TKE distribution at the orifice have been captured and are shown in Fig. 10. The impact of the recirculation region $C1$ is studied by considering the flow parameters at the periphery of the orifice.

Fig. 10(i) shows the locations and simulated values of τ_{max} for both heavy water and light water flows at all walls of the orifice. The periphery of the orifice or the orifice edge is located at the intersection of the upper walls ($U2, U3$) and ($L2, L3$). It is observed that the τ_{max} values for heavy and light water flow are almost same for all the walls except at the periphery. The light water flow has the maximum wall shear stress (τ_{max}) values at the orifice edge when comparing with that of the heavy water flow. Fig. 10(ii) shows the contours of TKE for *Re* = 2e+4. It is observed from both the Fig. 10(i) and (ii) is that the maximum value of these parameters is more at the orifice edge when compared with those values in the recirculation region. Therefore, a rise of maximum value of these parameters at the orifice periphery is due to the presence of upstream recirculation regions, sudden contraction in the geometry configuration and the heavy stress.

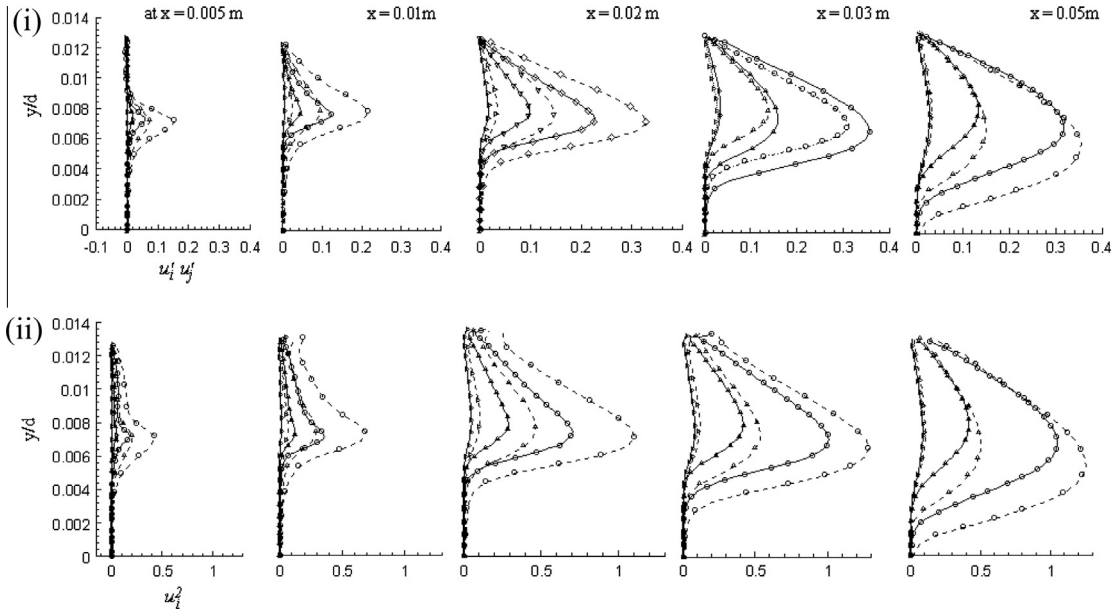

Fig. 9. Simulated radial profiles of (i) Reynolds shear stresses and (ii) normal stresses of heavy water (– – –) flow and light water (—) flow for three different *Re* values (▷ 2e+4, △ 4e+4 and ○ 6e+4) at the five axial locations.

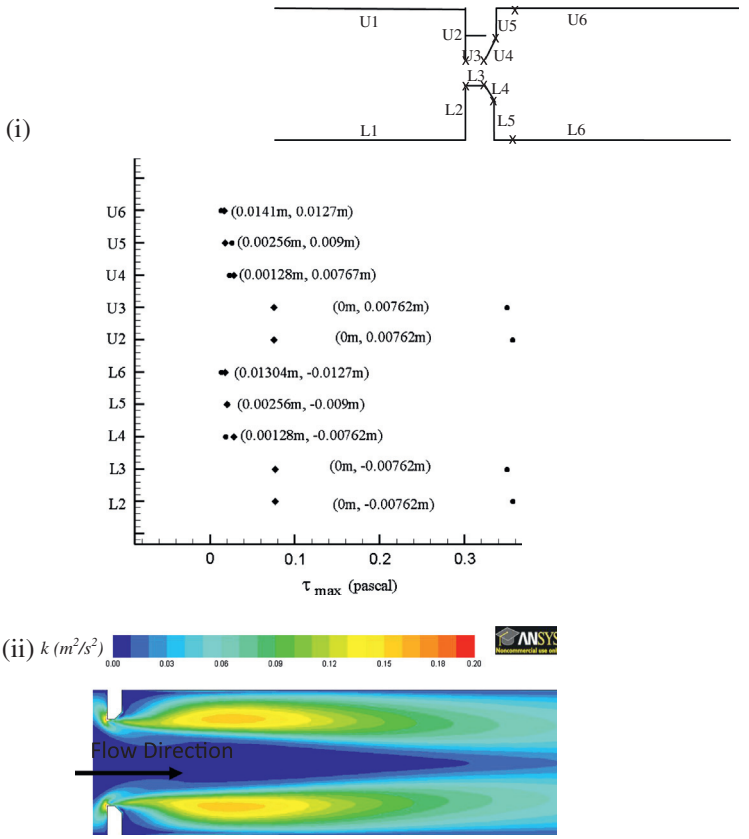

Fig. 10. (i) Locations and simulated values of τ_{max} (Pascal) for heavy (♦) and light (●) water flows. The insert figure shows the location (x) of τ_{max} (Pascal) in the orifice and (ii) simulated contours of TKE in an orifice for Re = 2e+4.

4.6. Sherwood number (Sh)

Several research works [23–25] showed that experimental data are often expressed in terms of *Sh*. The *Sh* is the non-dimensional representation of MTC and as function of the local hydrodynamic parameters and expressed as [18]

$$Sh = \frac{MTC' D}{D_f} \tag{8}$$

where D_f is the diffusion coefficient of iron in water and MTC' is defined as

$$MTC' = \frac{-D_f \left(\frac{\partial c}{\partial \boldsymbol{n}}\right)_w}{c_w - c_b} \tag{9}$$

in which $\boldsymbol{n}$ is the normal vector to the wall surface.

The experimental setup of Gammal et al. [8] has been considered to compare their results with the simulated *Sh* in an orifice. The value for D_f was taken as 6.45e−10 m^2/s and c_w and c_b was set to 3.46 and 0 kg/m^3, respectively. These values are similar to those considered by Gammal et al. [8]. The validation of *Sh* (Eq. (8)) is shown in terms of plots with the experimental results of Gammal et al. [8] and Coney [26] in an orifice with light water and heavy water flow for Re = 4e+4 and shown in Fig. 11. There is good agreement between the numerical and experimental axial profiles of *Sh*. The *Sh* increases steeply at the downstream of the orifice and reaches a maximum within the flow recirculation region, and then decreases as the flow evolves downstream. For the light water and heavy water the difference of *Sh* is less till it reaches the maximum value but thereafter slight difference is observed to have the more values for the heavy water flow than light water flow. This is due to the more concentration of ferrous ions for light water flow than for heavy water flow as shown in Fig. 12. Fig. 12, also presents the concentration of ferrous ions for both the fluids for different Sc values. It is observed from this figure is that the concentration of ferrous ions is decreasing as Sc increases. The behavior of the turbulent parameters observed from the Figs. 6–9 resemble the behavior of *Sh* in the recirculation region is observed from the Fig. 11. Gammal et al. [8] correlated the peak values of *Sh* with peak value of TKE. This correlation has been examined along with other turbulent parameters and observed that peak value exist at the center of the recirculation region.

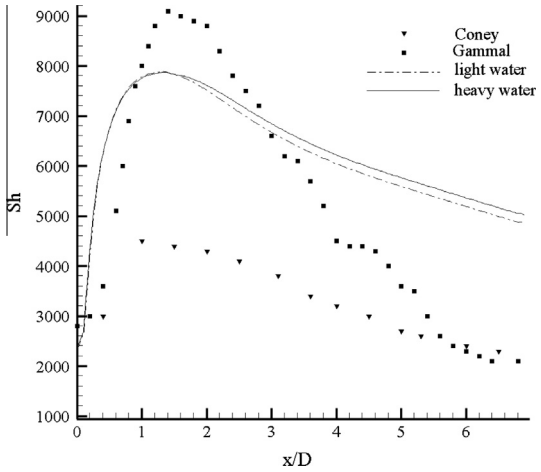

Fig. 11. Comparison of Sherwood number distribution of heavy water flow and light water flow with the experimental results of Coney [26] and Gammal [8] for *Re* = 4e+4.

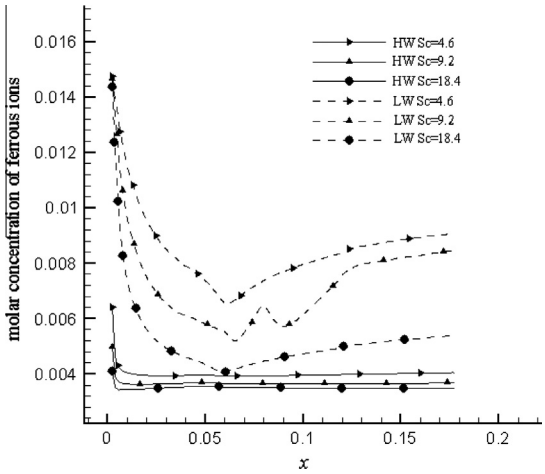

Fig. 12. Molar concentration of ferrous ions in heavy water (HW) flow and heavy water (LW) flow for different *Sc* values.

5. Conclusions

In the present study the steady, turbulent, two-dimensional flow of heavy water and light water in a cross sectional orifice is considered. The orifice was assumed to be made of carbon steel material and the flow was analyzed for three different Reynolds numbers, with constant Schmidt number and surface roughness values using the ANSYS Fluent 12.1 CFD software. These results were validated by a streamline portrait of the flow. The support for the proposed streamline portrait is provided by showing the corroborative numerical evidence. A good agreement was observed.

The Realizable k–ε model and Reynolds stress model have been employed to capture the turbulent flow and to calculate its parameters such as Turbulent kinetic energy (TKE), its dissipation rate (DR) and the Reynolds stresses accurately. For the different *Re* values, the zero shear stress lines are captured to describe the separation flow at the downstream of the orifice and it is observed that amplified *Re* value increased the reattachment length. The TKE, its DR and Reynolds stresses were calculated at the solid surface downstream of the orifice and also in the recirculation region at different axial locations along the transverse direction. It is observed that the TKE and both the shear and normal stresses attained a peak in the center line of the mixing layer and decreased in the vicinity of the wall. But the DR attains the maximum value at the wall. These radial stresses increased with the increased *Re* in each axial location. Higher turbulent kinetic energy and wall shear stress values observed at the periphery of orifice in comparison with that of values in the recirculation region. The locations having more values of wall shear stress and TKE are captured in an orifice for both heavy water and light water flows. In the recirculation region obtained with the heavy water flow have the higher turbulent parameter values in comparison with that of the light water flow, while this trend is reversed at the edge of the orifice. Also, to examine the FAC rate of heavy water flow and light

water flow in an orifice the *Sh* distribution has been calculated along the solid surface at the downstream of the orifice. The peak value of the *Sh* exists at the center of the recirculation region as for other turbulent parameters. From the present study the review of peak values of turbulence parameters and *Sh* in the orifice will help to locate the locations which are susceptible to FAC in the recirculation region and gives the intimation to pay attention at the orifice edge.

Acknowledgement

The financial support from the Board of Research in Nuclear Sciences, under BRNS/2009/36/70 – BRNS/2390, Department of Atomic Energy is gratefully acknowledged.

References

[1] Pietralik JM, Smith BAW. CFD applications to flow accelerated corrosion in feeder bends. In: Proceedings of ICONE-14, 14th international conference on nuclear engineering, Miami, FL, USA; July 17–20, 2006.
[2] Ahmed WH. Evaluation of the proximity effect on flow accelerated corrosion. Ann Nucl Energy 2010;37:598–605.
[3] Kanster W, Erve M, Henzel N, Stellwag B. Calculation code for erosion corrosion induced wall thinning in piping system. Nucl Eng Des 1990;119:431–8.
[4] Kain V, Roychowdhury S, Mathew T, Bhandakkar S. Flow accelerated corrosion and its control measures for the secondary circuit pipelines in Indian nuclear power plants. J Nucl Mater 2008;383:86–91.
[5] Kang DG, Jo JC. CFD application to the regulatory assessment of FAC-caused CANDU feeder pipe wall thinning issue. J Nucl Eng Technol 2008;40(1):37–48.
[6] Pietralik JM, Heppner KL. Flow-accelerated corrosion susceptibility prediction of recirculating steam generator internals. In: Proceedings of the 16th international conference on nuclear engineering, ICONE16, May 11–15, 2008, Orlando, Florida, USA, ICONE16-48630.
[7] Pietralik JM, Schefski CS. Flow and mass transfer in bends under flow-accelerated corrosion wall thinning conditions. J Eng Gas Turb Power 2011;133:012902-1–2-7.
[8] Gammal MAl, Ahmed WH, Ching CY. Investigation on wall mass transfer characteristics downstream of an orifice. J Nucl Eng Des 2012;242:353–60.
[9] Kim JW, Na MG, Park CY. Effect of local wall thinning on the collapse behavior of pipe elbows subjected to a combined internal pressure and in-plane bending load. J Nucl Eng Des 2008;238:1275–85.
[10] Kain V, Roychowdhury S, Ahmedabadi P, Barua DK. Flow accelerated corrosion: experience from examination of components from Indian nuclear power plants. Eng Fail Anal 2011;18(8):2028–41.
[11] Singh JL, Kumar Umesh, Kumawat N, Kumar Sunil, Kain V, Anantharaman S, et al. Flow accelerated corrosion of carbon steel feeder pipes, from pressurized heavy water reactors. J Nucl Mater 2012;429:226–32.
[12] Smith E, Artit R, Somravysin P, Promvonge. Numerical investigation of turbulent flow through a circular orifice. KMITL Sci J 2008;8(1).
[13] Shih TH, Liou WW, Shabbir A, Yang Z, Zhu J. A new k–ε eddy-viscosity model for high Reynolds number turbulent flows – model development and validation. Comput Fluids 1995;24(3):227–38.
[14] Durbin PA. A Reynolds stress model for near-wall turbulence. J Fluid Mech 1993;249:465–98.
[15] Versteeg HK, Malalasekera. An introduction to computational fluid dynamics the finite volume method. 2nd ed. New York: Longman; 1995.
[16] Brown GJ. Numerical simulation of separated flows in three – dimensional industrial geometries: a case study. Inter conf on CFD in mineral & metal processing and power generation; 1997. p. 157–64.
[17] ANSYS Fluent® version 12.1 Users Guide; 2009.
[18] Ahmed WH, Bello MM, Nakla MN, Sarkhi AA. Flow and mass transfer downstream of an orifice under flow accelerated corrosion conditions. J Nucl Eng Des 2012;252:52–67.
[19] Jana SC, Matacalfe G, Ottino JM. Experimental and a computational study of mixing in complex Stokes flows: the vortex mixing flow and multi cellular cavity flows. J Fluid Mech 1994;269:199–246.
[20] Drazin PG, Reid WH. Hydrodynamic stability. Cambridge University Press; 1981.
[21] Ma T, Wang S. Structure of 2D incompressible flows with the Dirichlet boundary conditions. Discrete Continuum Dynam Syst 2001;B1:29–41.
[22] Pope SB. Turbulent flows. Cambridge University; 2000.
[23] Berge P, Saint Paul P. Water chemistry of nuclear reactor systems. In: Proceedings of the British nuclear energy society, London; 1981. p. 19.
[24] Bouchacourt M, Remy FN. Proceeding of 3rd NACE international region management committee symposium, Cambridge, UK; 1991.
[25] Poulson B. Predicting the occurrence of erosion–corrosion, BSRIA; 1983.
[26] Coney M. CREL, Report RD/L/N197/80; 1980.